IEEE Access
Multidisciplinary ⋮ Rapid Review ⋮ Open Access Journal

Received 16 May 2024, accepted 19 June 2024, date of publication 26 June 2024, date of current version 3 July 2024.

Digital Object Identifier 10.1109/ACCESS.2024.3419082

RESEARCH ARTICLE

Diagnostics of Partial Discharge Measurements Utilizing Multi-Sensor Temporal Pulse Sequence Analysis

KAI ZHANG, (Student Member, IEEE), ALISTAIR REID, (Senior Member, IEEE), DAVID CLARK, (Member, IEEE), MICHAIL MICHELARAKIS, (Member, IEEE), AND A. MANU HADDAD, (Member, IEEE)
Advanced High Voltage Engineering Research Centre, School of Engineering, Cardiff University, CF24 3AA Cardiff, U.K.

Corresponding author: Kai Zhang (zhangk31@cardiff.ac.uk)

ABSTRACT This paper presents an improved temporal pulse sequence analysis (PSA) method for diagnosing partial discharge (PD) phenomena. The proposed method enables simultaneous high-resolution PD recognition across electrical sensors and ultra-high frequency antennae, facilitating the differentiation of defect types and the quantification of PD severity, as well as, their unique characteristics. This is achieved by utilizing advanced discrete-time integration techniques within two sensor measurement systems. Each PD event is time-stamped in post-processing, with a particular focus on analyzing charge-to-charge and ultra high frequency (UHF) energy-to-energy sequences analysis. The improved temporal PSA merits the advantages of a wide bandwidth of high-frequency current transformers and antennae to improve accuracy and efficiency. To conduct this method, a dual-sensor PD measurement circuit was set up to examine the protrusion on the ground side, the floating electrode, and the free-moving particle defects, which are potentially present in gas-insulated switchgear. Obtained results present dynamic PD variations in both time differences and magnitudes, establishing correlational PD patterns between sensors in a distinct manner. The application of the proposed method can serve as a reliable diagnostics approach for PD detection in gas-insulated switchgear and offer insights into underscoring PD phenomena itself.

INDEX TERMS Temporal pulse sequence analysis, discrete-time integration, partial discharge, dual-sensor PD measurement.

I. INTRODUCTION

The encapsulated design of high voltage alternating current (HVAC) gas-insulated systems (GIS) allows electrical conductors to be safely assembled within a compact structure, a feature that substantially minimizes land footprints. Despite being associated with high reliability, potential deficiencies due to manufacturing defects might threaten the dielectric strength and longevity of the GIS [1]. Typical defects such as protrusions on the ground electrode, free metallic particles [2], and floating electrodes [3] can create a region of the elevated electric field in the gaseous dielectric [4], which can, lead to partial discharge (PD). The assessment of the dielectric performance is often indicated through PD analysis, and with further diagnostics often revolving around PD-based methods by using conventional electric measurement and electromagnetic methods.

Two principal methodologies, phase-resolved partial discharge (PRPD) [5] and pulse sequence analysis (PSA) [6], [7], are often employed for the measurement and diagnostic evaluation of PD signals. Classic approaches regarding PRPD often make use of the 'apparent charge' or the discharge magnitude for PD diagnostics. These methods could reveal the severity of discharges however yield little information on the discharge processes. PSA, in concert with sensor-specific characterization, helped advance substantial understanding of

The associate editor coordinating the review of this manuscript and approving it for publication was Pavlos I. Lazaridis.

the correlation between individual pulses and the complex physical mechanisms of different PD sources [6], [7], [8], [9], [10], [11], [12].

The application of 'apparent charge' or discharge magnitude measurements is also feasible with PSA. Specifically, Madhar et al. [7] pioneered the development of weighted pulse sequence analysis (WePSA), while Vu-Cong et al. [13] explored its application in GIS by assessing the product or ratio of discharge quantity and time differences. Building upon the traditional electrical measurement methods outlined in IEC 60270 [14], there is significant research interest in combining electromagnetic techniques with electrical sensors. This integration aims to increase diagnostic sensitivity and provide a more comprehensive understanding of PDs. Madhar and Wenger [15] and Wenger et al. [16] implemented simultaneous ultra high frequency (UHF) antennae and electrical coupling measurement, applied with PSA algorithms, highlighting notable differences in data clusters between UHF voltages and apparent charges.

Enhancing the utilization of time stamps in pulse-pulse analysis could further enhance the diagnostics sensitivity between pre- and post-event fluctuations in PD magnitude and their respective time intervals, with a focus on charge-to-charge and UHF energy-to-energy sequences as contributed herein. Characteristics of PD signals, such as pulse shape, rise time, and duration, affect the apparent charge and influence the excited UHF voltage waveform. Traditional PSA/WePSA algorithms, which correlate charge/current with UHF voltage, may diminish the correlation between sensors and lead to inaccuracies if diagnostics rely solely on peak detection [8], [15]. These inaccuracies arise because the differences between the UHF voltage waveform and the current pulse shape are mainly due to the time-derivative effects of the antenna and resonances from adjacent objects.

Preserving the integrity of the UHF voltage waveform, and utilizing it to calculate UHF energy, is crucial. This preservation ensures that the UHF signals accurately reflect the influence of the PD current and enhance their correlations in the PSA. Such updates are also vital for advancing the development of a generalized WePSA post-processing method for wide bandwidth measurement systems, enabling the utilization of its high resolution to precisely characterize PD. Considering all of these factors, the refinement lies in implementing evenly spaced time division windows, a distinct departure from the reliance on even windows guided by minute-wise repetition rates for classification [11]. The mechanisms of stack clustering within updated WePSA can enhance the detection of subtle effects and potentially reduce unwanted noise. By integrating capacitive sensors and antennae into an impedance-matching circuit, WePSA could evolve into a temporal multi-sensor PSA approach based on discrete-time integration methods.

In the experimental setup, it was utilized specially designed high-frequency current transformers (HFCT) and UHF monopole antennae in a 50 Ω impedance-matching circuit design. These devices were configured for concurrent operation and aided in detecting PD activities from known defects. The synchronous operation of these devices, coupled with post-processing algorithms, allowed for an updated feature extraction method and comprehensive analysis of potential GIS defects. Three identical defects–protrusion on the ground side, floating electrode, and free-moving particle–were systematically introduced, with the ensuing PD events analyzed through the application of the temporal WePSA algorithm. This approach transforms raw PD signals into identifiable features, facilitating more accurate discrimination and analysis. The results correlation study enabled the differentiation of distinct sensor signatures and defect types, thereby enhancing the capability for subsequent defect identification within GIS systems. These enhancements are crucial for its potential application in industry settings, where reliable online PD detection is essential.

II. TEMPORAL PSA

The calculation of the apparent charge and UHF energy is advantageous due to its accuracy in representing the discrete-time integration of PD current (i.e., Q) or UHF pulse (i.e., E) in a single time window. As established by Reid et al. [17], the apparent charge Q and UHF energy E, might not always exhibit a proportional response to the same single PD current, which can be approximated by the Gaussian PD pulse equation:

$$I(t) = I_n \exp(\frac{-(t-t_0)^2}{2\sigma^2}), \tag{1}$$

where the PD current is symbolized as $I(t)$, and σ is the rise time of the pulse. While the peak magnitude of the current is employed to quantify the signal strength, it is clear from (1) that the peak current I_n is not the only factor that impacts Q. Additionally, UHF methods respond to the magnitude of the time-derivative of I_n (see Fig. 1).

These variations highlight the potential disparities in signals when analyzed using different methods, such as electric measurements and UHF antennae to reveal distinct details. Further, the temporal windows for the two quantities Q and E should be examined within individual frames, with a consistent time window being crucial for comparing apparent charge and UHF energy. For the time domain characteristics analysis, two time parameters are introduced here, as shown in Fig. 2. The first, denoted as τ_n, represents the absolute time differences between consecutive measurements, written as:

$$\tau_n = t_n - t_{n-1}. \tag{2}$$

The second parameter symbolized as T, corresponds to the uniform width of each time window, which is practically equivalent to the time per division setting (i.e., segmented triggering) on a digital storage oscilloscope (DSO). The selection of the time window for capturing PD pulses should be closely matched to the duration of these events, ensuring the window is sufficiently narrow to exclude multiple PD pulses from being recorded simultaneously. The time window for capturing PD pulses must be carefully selected to

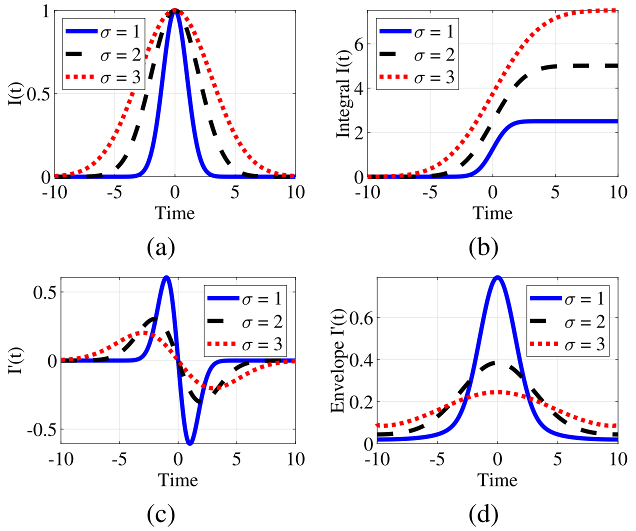

(a) (b) (c) (d)

FIGURE 1. Diagram of Gaussian Pulse equations with different rise time σ. (a) Original Gaussian equation. (b) The integral of current $I(t)$. (c) First time derivatives of $I(t)$. (d) Envelope of the first time derivatives $I(t)$.

encompass the 'duration' of these events with a margin. It should be narrow enough to prevent the simultaneous recording of multiple pulses but not so narrow as to cause signal clipping. Another advantage of segmented triggering is the prevention of unwanted noise occupying the majority of the dataset, which can impede post-processing speed. The fixed trigger level in a DSO serves as the counterpart to the settlement of t_n (see Fig. 2 for a visual representation). Each discrete time point corresponds to the time step Δt, and the time interval T is effectively the product of the number of time points and the time step, yielded as follows:

$$T = N\Delta t, \tag{3}$$

where N is the number of discrete time points in the time interval T. Physically, the increment or decrement between Q_n and Q_{n-1} represents the successive charge accumulation differences, given by:

$$\Delta Q_n(t) = \int_{t_n}^{t_n+T} I(t)\,dt - \int_{t_{n-1}}^{t_{n-1}+T} I(t)\,dt. \tag{4}$$

In Equation (4), $I(t)$ designates the current in a continuous form. This continuous formulation of (4) can be transformed into a discrete form, with derivation given as follows:

$$\Delta Q_n = \overbrace{\left(\sum_{n=1}^{N} I_n[i]\cdot\Delta t\right)}^{Q_n} - \overbrace{\left(\sum_{n=1}^{N} I_{n-1}[i]\cdot\Delta t\right)}^{Q_{n-1}}, \quad \text{for } i=[1,\ldots,N]. \tag{5}$$

In alignment with the operation of the DSO, which samples data before and after an event, and where t_n indicates the position of each window, the same values of τ_n and T can be applied to both charge difference and UHF energy difference conditions. With $Z_0 = 50\ \Omega$ impedance matching, ΔE_n is represented by (5), as follows:

$$\Delta E_n = \overbrace{\left(\sum_{n=1}^{N} \frac{V_n^2[i]}{Z_0}\cdot\Delta t\right)}^{E_n} - \overbrace{\left(\sum_{n=1}^{N} \frac{V_{n-1}^2[i]}{Z_0}\cdot\Delta t\right)}^{E_{n-1}}, \quad \text{for } i=[1,\ldots,N]. \tag{6}$$

To calculate the consecutive time differences between τ_n and τ_{n-1}, the existence of t_0 as shown in Fig. 2, as an index, is crucial for the time initialization. The charge difference at ΔQ_1 and the UHF energy difference of ΔE_1 should be excluded, as $t_0 = 0$ represented the pre-trigger of DSO for the time reference initiation, shown in Fig. 2. To apply given equations in real life, a high sampling frequency digitizer is required to minimize the data losses between divisions τ_n.

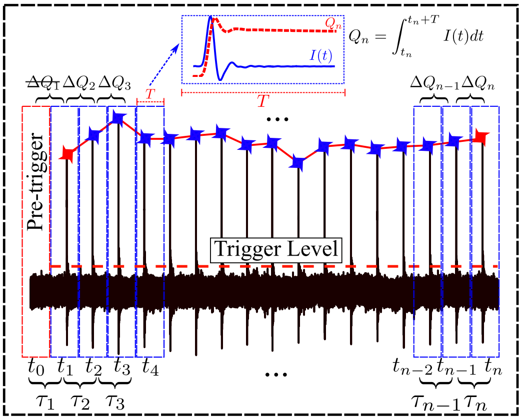

FIGURE 2. Diagram of updated successive pulses comparison model, associated with time/division oscilloscope setting.

The acquisition process outlined in Fig. 2 can be extended to the maximum memory of DSO. Here, τ_n, ΔQ_n, ΔE_n, $k_{\Delta Q_n}$, and $k_{\Delta E_n}$ denote the parameters derived from previous steps. Statistically, their interrelations are visualized through the plotting of:

$$k_{\tau_n} = \frac{\Delta Q_n \cdot \tau_n}{\Delta Q_n} = \tau_n. \tag{7}$$

$$k_{\Delta Q_n} = \frac{\Delta Q_n \cdot \tau_n}{\tau_n} = \Delta Q_n. \tag{8}$$

$$k_{\Delta E_n} = \frac{\Delta E_n \cdot \tau_n}{\tau_n} = \Delta E_n. \tag{9}$$

The scatter plot dispersion along the y-axis indicated the range of variation in $\Delta Q_n/\Delta E_n$ or τ_n with showing different k as different trends. For instance, different values of $k_{\Delta E_n}$ statistically illustrate the UHF energy magnitude distribution difference and the PD signal variability over time in the forms of ΔE_n. By utilizing the DSO-MATLAB interlink, this mathematical method can be implemented as a post-processing approach. This new integration of time parameters into the analysis is crucial; not only did it expand the range of the WePSA, enabling the incorporation of even time windows and multi-sensor suitability, this method also considerably reduces the acquisition of unwanted noise data, thereby enhancing efficiency.

III. EXPERIMENTAL SETUP

The practical application of the aforementioned mathematical model was the utilization of high sampling frequency and a wide bandwidth oscilloscope. In the experimental setup, a 4 GHz, 10 GS/s LeCroy Waverunner DSO was utilized in 50 Ω termination mode. For PD detection, a higher signal-to-noise ratio (SNR) of the HFCT and UHF antennae could be achieved by suppressing the noise threshold contained in signals by averaging the pre-energization. In this work, a total of 5000 time divisions having a duration of 20 ns, were established.

The 50 Hz AC test circuit with the multi-sensor configuration is illustrated in Fig. 3, adhering to the PD measurement setup found in IEC 60270 [18]. The pairing of a 1.8 $k\Omega$ series resistor with a 1 nF shunt capacitor acted as a low-pass filter for eliminating transients emanating from the HV amplifier. The data acquisition (DAQ) sensor-specific signal conditioning platform served as a multi-channel signal generator. This DAQ board was capable of generating a synchronized voltage ramp, subsequently producing an AC voltage that gets amplified in the Trek programmable HV amplifier. A PVM-10 voltage probe with a 2000:1 attenuation ratio was used to monitor voltage at the defect side.

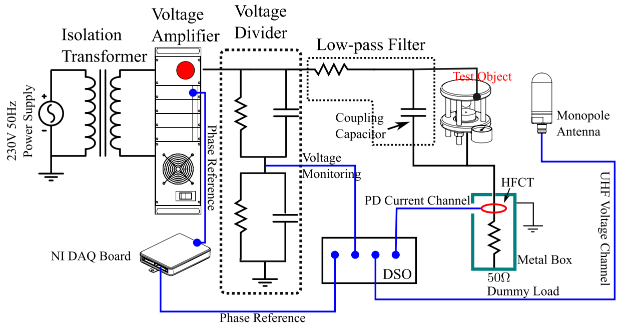

FIGURE 3. Diagram of test circuit setup. The test object and antenna were covered by a 1 m Faraday cage to mitigate interference and provide a favorable EM environment for UHF measurement. A designated HFCT was shielded in a metal box, and the whole signal loop of the HFCT and the UHF antenna followed an impedance-matching design.

In the experiments, fabricated test cells with defects were filled with selected technical air, composed of 21% oxygen and 79% nitrogen, and pressurized to 4 bar abs. As illustrated in Fig. 4, the following defects were examined:

1) **Needle tip defect on the grounding side:** This defect model incorporated a tip needle with a radius of 20 μm situated on the grounding side with a 5 mm gap. Such a configuration represents the presence of a sharp edge or a point that may occur in grounding components, leading to localized high electric fields in the form of negative corona discharge.
2) **Floating electrode defect:** In this scenario, a 1 mm gap was created between two points and the entire tips were bounded by polytetrafluoroethylene (PTFE), a material with a dielectric constant (ϵ_o) of 2.1. Additionally, there was an 8 mm gap present between the spherical test cell electrode. This defect simulates situations with loose screws floating between the HV conductor and ground enclosure that may be present in a GIS.
3) **Mobile particle between sphere surface:** This defect model contains a 3 mm mobile particle trapped between the spherical surfaces with a gap distance of 13 mm. The mobile particle can move under the influence of the electric field, and potentially cause intermittent or unpredictable ultimate insulation failure.

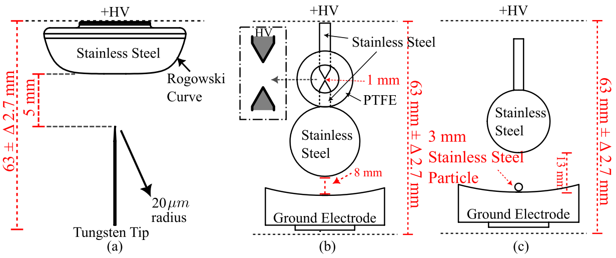

FIGURE 4. Diagram of test defects. From left to right: (a) plane-to-needle, (b) floating electrode, and (c) free-moving particle.

The calibration results for the PD detection circuit have been meticulously validated against IEC 60270 standards [18]. The system exhibited high precision in detecting PD apparent charge signals within the 10 pC to 10 nC range. This level of performance could be attributed to the effective 50 Ω impedance matching between the coupling devices in the PD detection signal loop. A representative time window was illustrated in Fig. 5. This arrangement accommodated a variety of pulse widths, and it helped to avoid potential issues such as signal clipping.

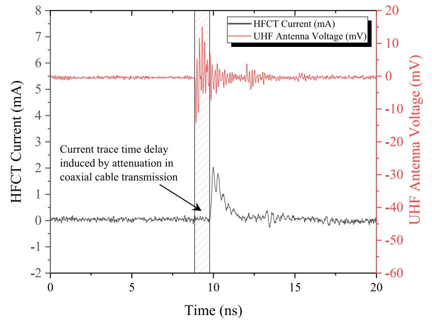

FIGURE 5. Example of comparative waveforms between UHF voltage trace and HFCT current trace within a single time window, derived from negative corona discharge for technical air pressurized to 4 bar abs.

IV. SENSOR CALIBRATION

IEC TS 62478 [14] states that the measurement technique employed in the UHF range may be implemented as a mode covering the entire bandwidth of the digitizer.

The inductive HFCT displays bandpass frequency response characteristics. Specifically, it adheres to the IEC 60270 and IEC TS 62478 standards for "wide-band PD instruments," encompassing a measurement bandwidth (Δf) within the high frequency (HF) to very high frequency (VHF) range. Michelarakis et al. [19] in the earlier work, reported an updated design of the HFCT that incorporates a 50 Ω impedance matching technique to enhance sensitivity. The calibration of each sensor should be conducted and assessed, independently.

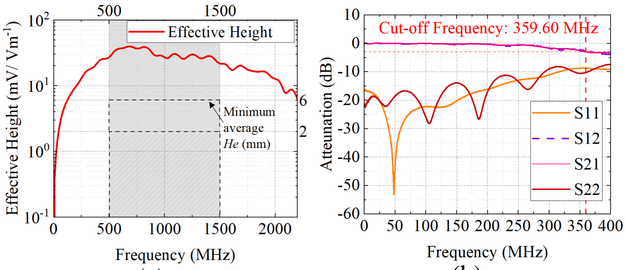

(a) (b)

FIGURE 6. Calibration results for the specified HFCT and UHF antenna: (a) Measurement of the UHF antenna's effective height; (b) Analysis of the HFCT's scattering parameters.

Dimensions of the UHF monopole antenna employed for this investigation are as follows: height 57.5 mm, radius 3.5 mm. For its calibration for PD detection, the gigahertz transverse electromagnetic (GTEM) cell as detailed by Judd et al. [20], was employed to measure the ratio (i.e., sensitivity, expressed in V/Vmm^{-1}) between the sensor's output voltage magnitude and the electric field strength (in V/mm). The chosen approach is corroborated by the effective height measurements depicted in Fig. 6(a), which demonstrate an average effective height above 30.9 mm for the capacitive type antenna. The antenna maintains full effectiveness for heights greater than 2 mm across the frequency range of 500 MHz to 1500 MHz. This range aligns with the criteria established in [21].

Assessing the scattering parameters (S-parameters) is critical to verify the transmission efficiency of the setup. To guarantee the integrity of the measurement configuration, the HFCT underwent precise calibration using a Rohde & Schwarz R&S ZVL vector network analyzer (VNA) capable of covering a frequency range from 9 kHz to 6 GHz. It is crucial for the reverse transmission losses (S_{12}) and transmission losses (S_{21}) parameters to approach 0 dB, which indicates that the signal is efficiently transmitted from Port 1 to Port 2 of the VNA with minimal attenuation. When these parameters are near 0 dB, S_{11} and S_{22} tend to exhibit high absolute values (below 0 dB), implying that the reflection of the signal back to its port of origin is negligible. The calibration results, illustrated in Fig. 6(b), confirmed that the HFCT has a frequency bandwidth up to 359.60 MHz at the -3 dB cutoff point ($f_{3\text{-dB}}$). Furthermore, the transmission losses, indicated by the S_{21} parameter, are minimal throughout the spectrum, with attenuation nearing 0 dB. It demonstrated the HFCT's effectiveness in managing a wide frequency range, especially within the VHF bands. These findings also suggested that the entire HFCT setup is capable of detecting current pulses with rise times τ_r as short as approximately 1 ns, calculated by the following equation:

$$\tau_r = \frac{0.35}{f_{3\text{-dB}}}. \tag{10}$$

V. RESULTS AND DISCUSSION

A. PARTIAL DISCHARGE INCEPTION VOLTAGE

The partial discharge inception voltage (PDIV) measurement in this study was conducted for all three defects under AC voltage in 4 bar abs. technical air, to support the temporal PSA diagnostics. The primary emphasis of this work was on the initiation events for the three defects at applied voltage slightly above their PDIV thresholds. In this way, an updated PDIV measurement could be developed with the introduction of time parameters t_n. Three distinct voltage ramps (see Table 1) were set, starting at 1 s. The resultant PDIVs are reported and demonstrated in Fig. 7 with 20 measurements per defect.

TABLE 1. Ramp voltage configuration and PDIVs of different defects.

Defect types	Testing ramp voltage applications (s × V/s)	Average PDIV (kV)	Normalized ramp peak voltage (p.u.)
Plane-to-needle	25 × 150	3.42	1.10
Floating electrode	50 × 275	12.73	1.10
Free-moving particle	40 × 500	18.59	1.10

Applying the PDIV definition outlined in IEC 60270 [18], every test is applied increasing voltage with a unique time signature to identify the lowest voltage that triggered the first PD event. This approach reduced the variability of PD behaviors, particularly in scenarios where PDIVs were dominated by different electric fields, such as under the free-moving particle and the floating electrode (see Fig. 7) configurations. The average PDIVs in Table 1 were key in setting the ramp peak value to around 1.1 p.u. PDIVs for different defects.

B. NEGATIVE CORONA DISCHARGE

In order to gather additional details on corona discharge pulses, the temporal PSA technique was employed for further processing and analysis of the discharge data. Figs. 8–9 depicted the variations in the ratio of apparent charge to UHF energy over time, as well as the charge/UHF energy differences that arose from the negative corona discharge within the plane-to-needle defect. To explain the PD distribution in Figs. 8–9, when the plane electrode becomes positively charged, free electrons are drawn towards it. During their movement, these electrons may bombard neutral

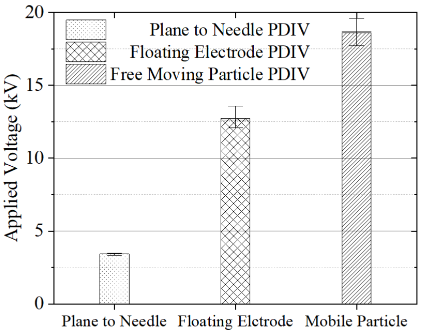

FIGURE 7. PDIV results of three different defects under 0.4 MPa pressurized technical air with AC voltage application.

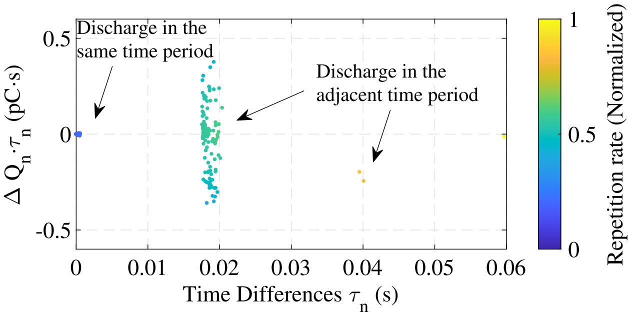

(a) Consecutive time differences (x-axis) versus charge-weighted differences (y-axis).

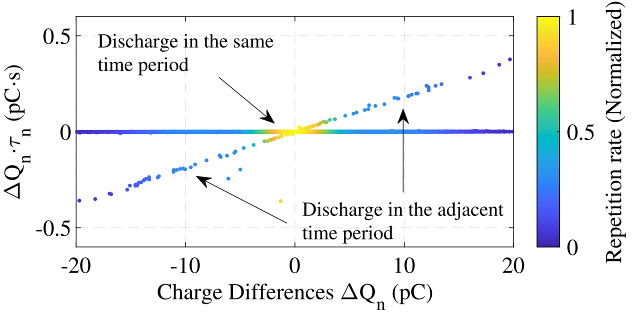

(b) Consecutive charge differences (x-axis) versus time-weighted differences (y-axis).

FIGURE 8. Temporal PSA pattern of negative corona discharges at AC voltage monitored by the HFCT.

molecules. Such collisions can result in different outcomes: electrons may attach to these molecules, forming negative ions, or they may excite the molecules, ultimately leading to ionization. The negative corona discharge, once generated, might conduct a high repetition rate and low-energy discharge process. These phenomena could be observed in multiple instances of discharge occurring within nearly identical periods, specifically showing the k_{τ_n}, which are close to zero. This was illustrated in Figs. 8(a) and 9(a). Additionally, the phenomena were evident through the high repetitive, low amplitude rates of charge or energy change, representing $k_{\Delta Q_n}$ and $k_{\Delta E_n}$, as depicted in Figs. 8(b) and 9(b).

Minor discrepancies observed between Fig. 8 and Fig. 9 revealed differences in charge and UHF energy within the identical time window periods. These variations were indicative of the trends in corona discharge development monitored by two sensors. In Fig. 8 (a), monitored by the HFCT, most of the scatter points were clustered within $\tau_n \approx 0.02$ s. However, the dense distribution of UHF energy scatter $\tau_n \approx 0$ s suggested a reduced time interval between events within the same detection period could be monitored utilizing antennae, indicating a better PD recognition ability of the unconventional UHF measurement. Following the interpretation presented in [11] and [22], stochastic corona discharge could be influenced by the polarity of pulse sequences, often resulting in the formation of quasi-symmetric PSA patterns. The magnitude differences under Fig. 8(b) and Fig. 9(b) revealed recognition capabilities between sensors. The noticeable patterns in charge differences illustrated the development of discharge magnitude over a consistent period (approximately 0 – 20 pC), characterized by irregular pulse glows and variation of discharge magnitudes [23], [24]. This could be compared as a reference since very close intervals between UHF events (0 – 0.005 pJ) in general indicate a higher resolution of the monitoring process. Fig. 9(a) indicated more unsymmetrical adjacent UHF energy distribution, i.e., more detailed stable discharge period and transit period, in which PDs were generated in the same experimental setup.

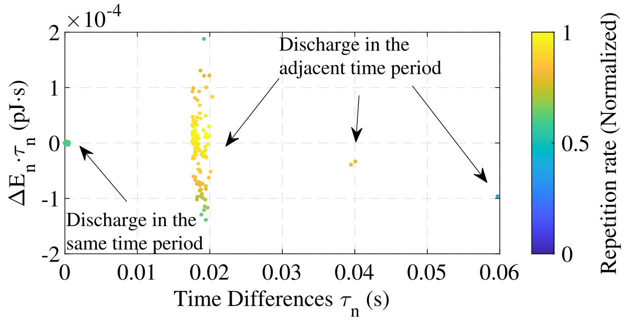

(a) Consecutive time differences (x-axis) versus UHF energy-weighted differences (y-axis).

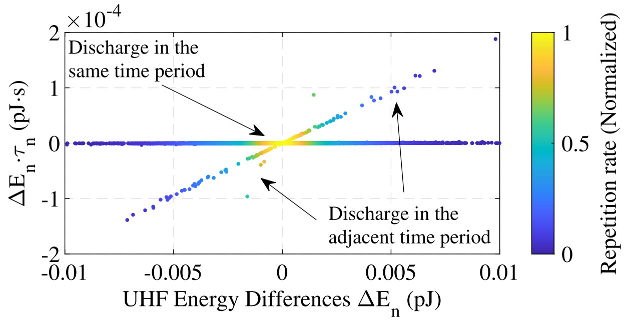

(b) Consecutive UHF energy differences (x-axis) versus time-weighted differences (y-axis).

FIGURE 9. Temporal PSA pattern of negative corona discharges at AC voltage monitored by the UHF antenna.

Notably, the similarities in the patterns of apparent charge and UHF energy suggested that negative corona discharges can be accurately detected by both sensing methodologies,

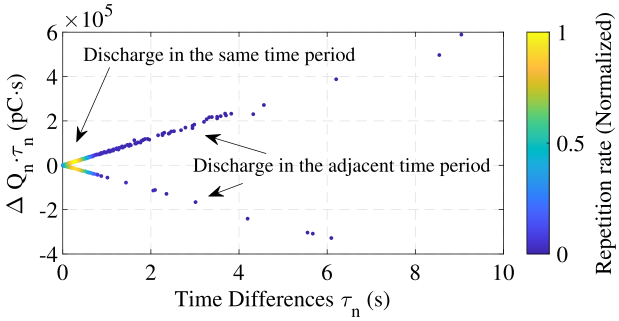

(a) Consecutive time differences (x-axis) versus charge-weighted differences (y-axis).

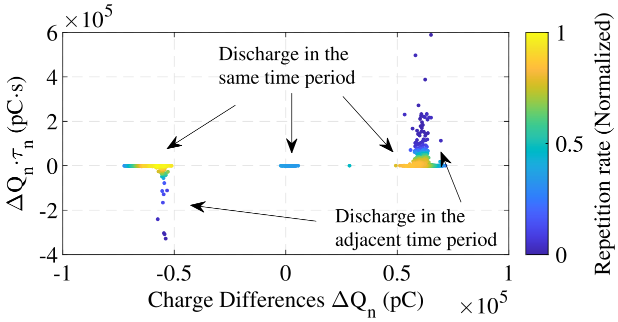

(b) Consecutive charge differences (x-axis) versus time-weighted differences (y-axis).

FIGURE 10. Temporal PSA pattern of floating electrode discharges at AC voltage monitored by the HFCT.

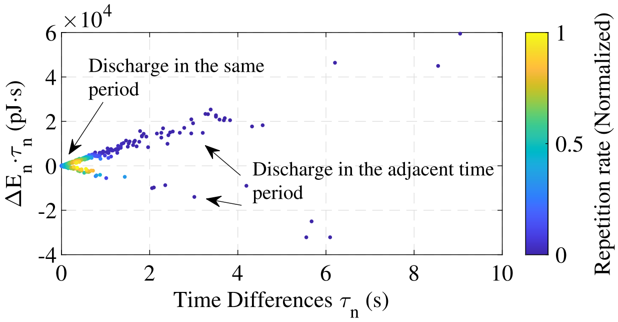

(a) Consecutive time differences (x-axis) versus UHF energy-weighted differences (y-axis).

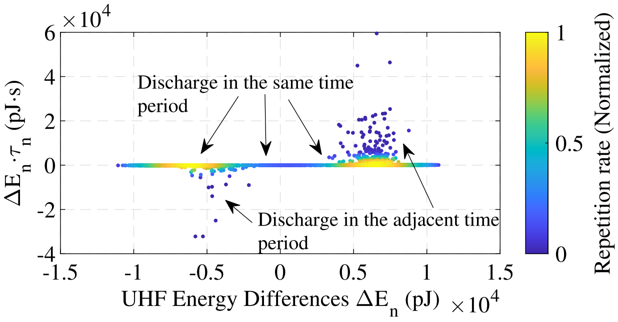

(b) Consecutive UHF energy differences (x-axis) versus time-weighted differences (y-axis).

FIGURE 11. Temporal PSA pattern of floating electrode discharges at AC voltage monitored by the UHF antenna.

underscoring the utility of dual-sensor analysis in capturing typical PD characteristics when the signal variation and emitted energy were not significant.

C. FLOATING ELECTRODE

In the case of the floating electrode defect as shown in Fig. 4(c), three distinct clusters of full discharges are observed. These discharge events occurred in the needle-to-needle gap (i.e., primary gap), resulting from a significant charge accumulation on the electrode which is then discharged to the ground. This process is initiated when the voltage across the primary gap reaches the breakdown threshold, causing a temporary bridge across the gap in the form of sparks [25]. Upon energization, the floating body loses its electrical neutrality and starts to accumulate charges. When the voltage across the gap exceeds the corona inception threshold, the effect of primary gap conduction leads to a further increase of the rod-plane gap's electric field and initiates a charge-discharge process [26], [27]. The presence of such phenomena could potentially affect the amplitude differences of the PD events, as demonstrated in Fig. 10 and Fig. 11. Hutzler [28] identified polarity-dependent effects of discharges in the needle-to-needle gap. They noted that variations in magnitude are due to field distribution in the test object, which changes with different AC half-cycle polarities. Fig. 10(a) and Fig. 11(a) simultaneously indicated such phenomena in the form of repetition differences in adjacent periods, owing to that there were more events in the positive half cycle. The repetition rate remained a viable indicator, capable of revealing the presence of low-amplitude corona discharge phenomena in the rod-plane gap. As verified in Fig. 10(b), if the critical electric field at the top of the primary electrode sustains a repetitive discharge current, the scatter plots illustrated a greater frequency of events occurring around $\Delta Q_n \approx 65$ nC than $\Delta Q_n \approx -65$ nC in adjacent periods. When contrasted with the outcomes of the apparent charge differences, the statistical variances might provide a more effective measure for identifying the evolution paths of PD sources. This was displayed by the reduced differences in UHF energy across consecutive periods $k_{\Delta E_n}$, as shown in Fig. 10(a) between $\tau_n \approx 0-5$ s. A more pronounced increase in the time intervals between consecutive discharge events could be observed, and trajectories of floating electrode discharges were more obvious. Compared with HFCT results, more discharges in the adjacent period were detected by the UHF antennae, indicating a wider array of discharge anomalies. The UHF energy scatter plot, in Fig. 11(b) indicated a high-frequency region of discharge events with magnitudes around $\Delta E_n \approx \pm 8$ nJ, which was comparable to the observations in Fig. 10(b). The enhanced sensitivity observed in UHF antennas did not negate the significance of HFCT sensors as a conventional method of measurement. Rather, the employment of correlation analysis substantively augments the accuracy in identifying the implications of high PD intensity originating from floating electrodes. In the aspect of PD magnitudes, these findings suggested that the presence of a floating electrode defect can significantly impact the insulation condition of the GIS.

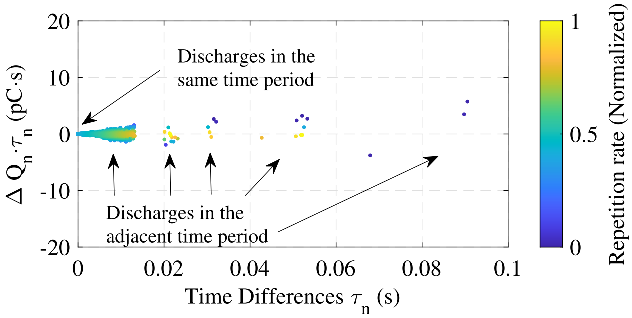

(a) Consecutive time differences (x-axis) versus charge-weighted differences (y-axis).

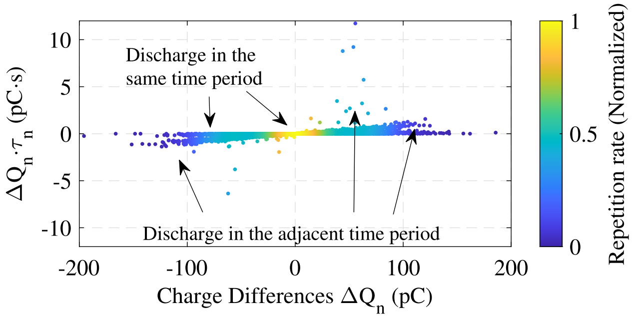

(b) Consecutive charge differences (x-axis) versus time-weighted differences (y-axis).

FIGURE 12. **Temporal PSA pattern of the free moving particle discharges at AC voltage monitored by the HFCT.**

D. FREE MOVING PARTICLE

When the 3 mm ball bearing shifts within the test cell, it generates an intense, non-uniform electric field. If the ball bearing is stationary, it predominantly experiences the 'lift-up' force, a phenomenon elucidated by Cooke et al. [29]. During their initial lift-off, the particle of this size tends to travel a constrained distance within half of an AC cycle. As a consequence, they bounce back off the lower electrode, only crossing the complete gap when subjected to elevated voltages [29], [30]. This alteration in the ball bearing's movement, synchronized with the AC voltage cycle, can dynamically modify the reduced electric field near its curved surface, thereby affecting the ionization and electron attachment processes in the air. The resulting field ionization might generate successive and magnitude-varied discharge events subject to the inhomogeneous electric field distribution between the rod-sphere electrodes. Consequently, the conductive ball bearing's movement on the sphere electrode results in voltage-dependent PD phenomena, characterized by a degree of randomness.

The physical interpretation behind the sporadic movement of the metallic particle could be non-trivial to qualify. However, the charge/UHF energy differences and time differences, as shown in Figs. 12–13, could display the PD magnitude and repetitve rate variations. Distinct scatters could be observed compared with the aforementioned defects. In the plots of time differences versus weighted quantities, as seen in Fig. 12(a) and Fig. 13(a), it was observed that during identical time intervals, there are numerous instances of low PD magnitudes. Nevertheless, these were accompanied by more repetitive events with different and specific time gap signatures ($\tau_n \approx 0.01, 0.022, 0.03, 0.042$ s), and a progressively increasing magnitude with wider time intervals and lower repetition. For an unpredictable discharge source, magnitude fluctuation and several time intervals can also be examined by dispersion k_{τ_n}. The occurrence of particle bouncing, particularly notable with rounded particles under AC voltage of two polarities and in conditions of high gas pressure, leads to the creation of a pseudo-resonance state of motion as a result of this effect [11]. This consistency between magnitude and time became more pronounced when observing the particle trajectories in Fig. 13(b), which displayed multiple lines of dispersion. These trajectories led to the formation of several distinct charge clusters, showcasing fluctuations in charge magnitude ranging from $\Delta Q_n \approx -150$ pC to $\Delta Q_n \approx 150$ pC. The consecutive UHF energy differences in Fig. 13(b) clearly capture the pattern's relationship with particle motion with a small and distinct energy variation ($\Delta E_n \approx \pm 15$ pJ), which might have been due to rapid energy fluctuations stemming from the complex electric field. Comparing and analyzing certain charge/UHF temporal PSA patterns in Fig. 12 and Fig. 13, especially the pronounced distinctions between different cluster stacks,

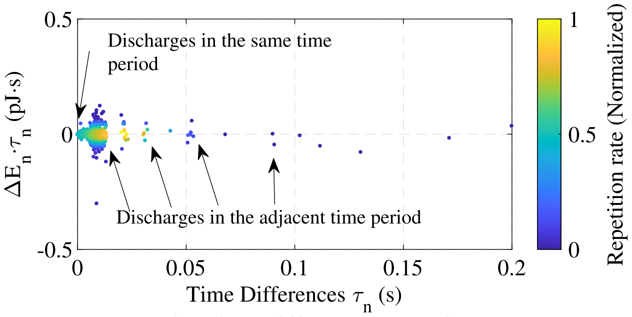

(a) Consecutive time differences (x-axis) versus UHF energy-weighted differences (y-axis).

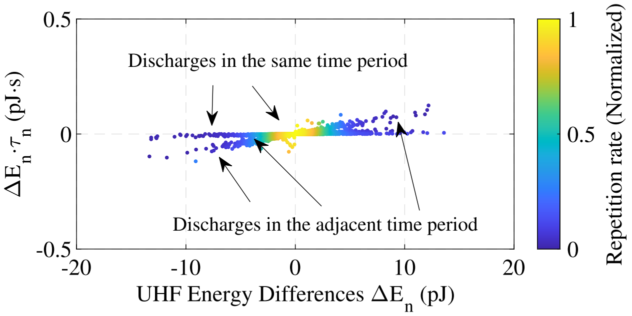

(b) Consecutive UHF energy differences (x-axis) versus time-weighted differences (y-axis).

FIGURE 13. **Temporal PSA pattern of the free moving particle discharges at AC voltage monitored by the UHF antenna.**

can serve as markers for the unique distribution of mobile contaminants within the GIS.

VI. CONCLUSION

This paper introduced a refined temporal PSA algorithm, establishing a connection by applying time parameters between consecutive UHF energy and apparent charge outcomes from three prevalent GIS defects. A feature of this time-based multi-sensor PSA is evaluating the distribution of the ratio clusters for specialized defects. Under 1.1 p.u. of their PDIVs, distinct PD result patterns simultaneously demonstrated the availabilities of both conventional electrical measurement and UHF antennae with temporal PSA algorithm. The key findings from these experiments, derived through concurrent measurements and the application of the temporal PSA algorithm, can be encapsulated in the following essential points:

1) Building upon WePSA, the enhanced temporal PSA exhibited broader applicability and PD results correlation in incorporating various sensors, particularly traditional and non-traditional PD measurement techniques.
2) The presence of a range of values for $k_{\Delta Q_n}$, $k_{\Delta E_n}$, and k_{τ_n} facilitated the evaluation and examination of the discharge's behaviors between defects, particularly through the cluster distribution method with quantified values.
3) In the vicinity of the inception voltage of defects, the PD behavior associated with various defects was observed to be more intricately monitored using the UHF antenna. In contrast, the HFCT demonstrated a heightened ability to differentiate PD clusters based on pulse shapes, offering a more distinguishable analysis for further study.
4) Setting up the time-division DSO with a trigger level above the noise threshold can effectively reduce the inclusion of noise data during the post-processing stage. However, a longer duration measurement for high-frequency discharges, like negative corona discharge, necessitates a larger memory capacity in the DSO.

Application of the purposed temporal PSA in realistic GIS may involve the development and integration of electromagnetic wave propagation models for improving PD detection sensitivity, alongside the comparison of temporal PSA results in this work. This would facilitate a comprehensive understanding of observed signal attenuation and thereby enhance the reliability and practical applicability of the temporal PSA algorithm in real-world scenarios.

REFERENCES

[1] G. A. Hussain, W. Hassan, F. Mahmood, and J. A. Kay, "Partial discharge based risk assessment framework for MV switchgear containing electrical defects," *IEEE Trans. Ind. Appl.*, vol. 59, no. 6, pp. 7868–7875, Dec. 2023.

[2] J. Sun, N. Wu, Y. Fan, D. Lei, S. Yang, X. Guo, H. Wang, and S. Song, "Partial discharge characteristics of free moving metal particles in gas insulated systems under DC and AC voltages," *IET Gener., Transmiss. Distribution*, vol. 17, no. 5, pp. 1047–1058, May 2022.

[3] J. Gao, L. Wang, S. Wu, C. Xie, Q. Tan, G. Ma, H. Tueraili, and B. Song, "Effect of a floating conductor on discharge characteristics of a long air gap under switching impulse," *J. Electrostatics*, vol. 114, Nov. 2021, Art. no. 103629.

[4] G. A. Hussain, W. Hassan, F. Mahmood, M. Shafiq, H. Rehman, and J. A. Kay, "Review on partial discharge diagnostic techniques for high voltage equipment in power systems," *IEEE Access*, vol. 11, pp. 51382–51394, 2023.

[5] M. Choudhary, M. Shafiq, I. Kiitam, I. Palu, W. Hassan, and P. P. Singh, "Investigation of partial discharge characteristics in XLPE cable insulation under increasing electrical stress," *Eng. Failure Anal.*, vol. 158, Apr. 2024, Art. no. 108006.

[6] P. Wenger, M. Beltle, S. Tenbohlen, U. Riechert, and G. Behrmann, "Combined characterization of free-moving particles in HVDC-GIS using UHF PD, high-speed imaging, and pulse-sequence analysis," *IEEE Trans. Power Del.*, vol. 34, no. 4, pp. 1540–1548, Aug. 2019.

[7] S. Abdul Madhar, P. Mraz, A. Rodrigo Mor, and R. Ross, "Empirical analysis of partial discharge data and innovative visualization tools for defect identification under DC stress," *Int. J. Electr. Power Energy Syst.*, vol. 123, Dec. 2020, Art. no. 106270.

[8] S. M. K. Azam, M. Othman, H. A. Illias, T. A. Latef, D. Fahmi, W. J. K. Raymond, W. N. L. W. Mahadi, A. K. M. Z. Hossain, M. Z. A. A. Aziz, and A. Ababneh, "Unknown PD distinction in HVAC/HVDC by antenna-sensor with pulse sequence analysis," *Alexandria Eng. J.*, vol. 91, pp. 457–471, Mar. 2024.

[9] R. Patsch, "Pulse sequence analysis—What does it tell us about multiple discharge sites?" in *Proc. 7th Int. Conf. Dielectr. Mater., Meas. Appl.*, Bath, U.K., 1996, pp. 133–136.

[10] J. Song, Z. Lv, Y. Li, Z. Wu, K. Wu, and Y. Cheng, "Analysis of polypropylene surface discharge characteristics with pulse sequence analysis," in *Proc. IEEE Conf. Electr. Insul. Dielectr. Phenomena (CEIDP)*, Denver, CO, USA, Oct. 2022, pp. 495–498.

[11] A. Pirker and U. Schichler, "Partial discharge measurement at DC voltage—Evaluation and characterization by NoDi∗ pattern," *IEEE Trans. Dielectr. Electr. Insul.*, vol. 25, no. 3, pp. 883–891, Jun. 2018.

[12] M. Geske, C. Neumann, T. Berg, and R. Plath, "Assessment of typical defects in gas-insulated DC systems by means of pulse sequence analysis based on UHF partial discharge measurements," in *Proc. VDE High Voltage Technol. (ETG-Symposium)*. Berlin, Germany: VDE Verlag, Nov. 2020, pp. 1–8.

[13] T. Vu-Cong, C. Toigo, F. Jacquier, A. Girodet, M. N. Tuczek, U. Riechert, and A. R. Mor, "Long-term partial discharge behavior of protrusion defect in HVDC GIS," *IEEE Trans. Dielectr. Electr. Insul.*, vol. 29, no. 6, pp. 2294–2302, Dec. 2022.

[14] *High Voltage Test Techniques—Measurement of Partial Discharges By Electromagnetic and Acoustic Methods*, Standard IEC TS 62478, Int. Electrotechnical Commission, Geneva, Switzerland, 2016.

[15] S. A. Madhar and P. Wenger, "Simultaneous electrical and UHF measurement of DC-PD from point-plane defect," in *Proc. 21st Int. Symp. High Voltage Eng.*, vol. 599, B. Németh, Ed. Cham, Switzerland: Springer, 2020, pp. 991–1003.

[16] P. Wenger, S. Abdul Madhar, and M. Beltle, "Simultaneous electrical, UHF, current and optical PD measurements on floating potential under DC stress," in *Proc. IEEE Conf. Electr. Insul. Dielectr. Phenomena (CEIDP)*, Richland, WA, USA, Oct. 2019, pp. 287–290.

[17] A. J. Reid, M. D. Judd, R. A. Fouracre, B. G. Stewart, and D. M. Hepburn, "Simultaneous measurement of partial discharges using IEC60270 and radio-frequency techniques," *IEEE Trans. Dielectr. Electr. Insul.*, vol. 18, no. 2, pp. 444–455, Apr. 2011.

[18] *High-Voltage Test Techniques: Partial Discharge Measurements*, Standard IEC 60270, Int. Electrotechnical Commission, Geneva, Switzerland, 2000.

[19] M. Michelarakis, P. Widger, A. Beroual, and A. M. Haddad, "Electrical detection of creeping discharges over insulator surfaces in atmospheric gases under AC voltage application," *Energies*, vol. 12, no. 15, p. 2970, Aug. 2019.

[20] M. D. Judd, O. Farish, and J. S. Pearson, "UHF couplers for gas-insulated substations: A calibration technique," *IEE Proc., Sci., Meas. Technol.*, vol. 144, no. 3, pp. 117–122, May 1997.

[21] M. D. Judd, L. Yang, and I. B. B. Hunter, "Partial discharge monitoring of power transformers using UHF sensors. Part I: Sensors and signal interpretation," *IEEE Elect. Insul. Mag.*, vol. 21, no. 2, pp. 5–14, Apr. 2005.

[22] X. Meng, X. Li, and T. Lu, "Statistical properties of corona current pulses in rod-plane air gap under AC–DC composite voltages," *IEEE Trans. Dielectr. Electr. Insul.*, vol. 31, no. 1, pp. 212–221, Feb. 2024.
[23] Y. Zhang, Q. Xia, Z. Jiang, and J. Ouyang, "Trichel pulse in various gases and the key factor for its formation," *Sci. Rep.*, vol. 7, no. 1, p. 10135, Aug. 2017.
[24] B. R. T. Cotts, K. L. Graf, and W. H. Bailey, "Electromagnetic interference considerations for electrical power systems," in *The Power Grid*, B. W. D'Andrade, Ed. New York, NY, USA: Academic, 2017, pp. 137–170.
[25] K. Feser, "Influence of corona discharges on the breakdown voltage of airgaps," *Proc. Inst. Electr. Eng.*, vol. 118, no. 9, p. 1309, 1971.
[26] F. Roman, V. Cooray, and V. Scuka, "Corona from floating electrodes," *J. Electrostatics*, vol. 37, nos. 1–2, pp. 67–78, May 1996.
[27] J. Gao, T. Ding, Y. Fang, K. Liu, S. Wu, E. Li, L. Wang, and A. Cavallini, "Experimental investigation on the formation mechanism of the lowest breakdown voltage area in a long air gap containing a floating conductor under positive switching impulses," *IEEE Trans. Dielectr. Electr. Insul.*, vol. 31, no. 1, pp. 560–567, Feb. 2024.
[28] B. Hutzler, "Switching impulse strength of air gaps containing a metallic body at floating potential," in *Proc. 5th ISH*, Braunschweig, Germany, 1987, p. 11.1.
[29] C. M. Cooke, R. E. Wootton, and A. H. Cookson, "Influence of particles on AC and DC electrical performance of gas insulated systems at extra-high-voltage," *IEEE Trans. Power App. Syst.*, vol. PAS-96, no. 3, pp. 768–777, May 1977.
[30] J. Wang, Q. Hu, Y. Chang, J. Wang, R. Liang, Y. Tu, C. Li, and Q. Li, "Metal particle contamination in gas-insulated switchgears/gas-insulated transmission lines," *CSEE J. Power Energy Syst.*, vol. 7, no. 5, pp. 1011–1025, Sep. 2021.

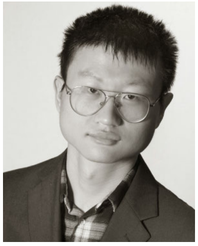

KAI ZHANG (Student Member, IEEE) received the Master of Science degree in electric energy systems from Cardiff University, U.K., in 2020, where he is currently pursuing the Ph.D. degree in high voltage engineering. During his time as a master's student, he was a Student Representative in electric energy system project with Cardiff University, from 2020 to 2021. He is engaged in research with the Advanced High Voltage Engineering Research Centre, Cardiff University. His research interests include plasma phenomena, partial discharge in gas-insulated high-voltage systems, multi-sensor diagnostics methods, ultra-high frequency diagnostics, and the influence of HVDC harmonics. He is also a member of IET.

ALISTAIR REID (Senior Member, IEEE) received the B.Eng. degree (Hons.) in electrical and mechanical engineering from the University of Strathclyde, in 2004, and the Ph.D. degree, in 2007, for research on partial discharge monitoring. He conducted postdoctoral research with the Institute for Energy and Environment, University of Strathclyde, from 2007 to 2011, studying advanced radiometric techniques for partial discharge detection and diagnostic monitoring. He is currently a Senior Lecturer with the School of Engineering Researching Diagnostic Monitoring Techniques, Advanced High Voltage Engineering Research Group, Cardiff University. His interests include energy harvesting, RF sensors, and condition monitoring of gas-insulated high-voltage systems.

DAVID CLARK (Member, IEEE) received the B.Eng. and Ph.D. degrees in electrical and electronic engineering from Cardiff University, Cardiff, U.K., in 2007 and 2012, respectively. In 2012, he was a Research Associate and an Academic Post with Cardiff University, in 2014. He is currently a Senior Lecturer of high voltage and high current engineering with Cardiff University. His research interests include high-voltage insulation systems for aviation, lightning direct effects, computational electromagnetics, and earthing in electrical energy systems. He is also a member of IET and a fellow of the Higher Education Academy.

MICHAIL MICHELARAKIS (Member, IEEE) received the M.Eng. degree in electrical and computer engineering from the Democritus University of Thrace, Greece, the M.Sc. degree in electric power engineering from the KTH Royal Institute of Technology, Sweden, and the Ph.D. degree from Cardiff University, Cardiff, U.K. He is currently a Research Associate with the Advanced High Voltage Engineering Research Centre (AHIVE), Cardiff University. His research interests include eco-friendly insulating gases, surface and partial discharge properties, and electromagnetic computations.

A. MANU HADDAD (Member, IEEE) received the first degree in electrical engineering from Ecole Nationale Polytechnique, Algiers, in 1985, and the Ph.D. degree in high voltage engineering from Cardiff University, Cardiff, U.K., in 1990. He is currently a Professor of electrical engineering with Cardiff University, with responsibility for research in high voltage engineering. He has authored or coauthored an IET-Power Series Book on *Advances in High Voltage Engineering* (IET, 2004). His research interests include overvoltage protection, insulation systems, insulation coordination, and earthing of electrical energy systems. He is a member of CIGRE working groups and a member of BSI PEL1/2, IEC TC37. He serves on the scientific committees of several international conferences.

• • •